PAPER

Check for updates

A co-delivery nanoplatform for a lignan-derived compound and perfluorocarbon tuning IL-25 secretion and the oxygen level in tumor microenvironments for meliorative tumor radiotherapy†

Zhenyu Duan,[a] Qiang Luo,[a] Lei Gu,[a] Xiaoling Li,[a] Hongyan Zhu,*[a] Zhongwei Gu, [ID] [a] Qiyong Gong,[a,b] Hu Zhang[c] and Kui Luo [ID] *[a,b]

A hypoxic environment in tumors hampers the therapeutic efficacy of radiotherapy. Moreover, radiotherapy, a localized treatment technique, can barely control tumor metastases. Herein, poly(lactic-*co*-glycolic acid) was used to encapsulate perfluorocarbon (PFC) for increasing the oxygen level and a lignan-derived compound (Q1) for enhancing IL-25 secretion from fibroblasts, thereby boosting the radiotherapeutic effect on local and distant tumors. The prepared co-delivery nanoplatform, PFC-Q1@PLGA, has a nanoscale size of around 160 nm and a negative zeta potential (about −13 mV). PFC-Q1@PLGA treatment leads to an arrest of the G2 phase (4n) in the cell cycle and reduces the mitochondria membrane potential. A high expression level of IL-25 in fibroblasts is detected after the cells are treated with PFC-Q1@PLGA, which increases the late apoptosis percentage of 4T1 cells after treatment with IL-25-containing conditional medium from fibroblasts. The oxygen level in tumors is significantly promoted to about 52.3% after injection of oxygen-saturated PFC-Q1@PLGA (O$_2$), which is confirmed from the functional magnetic resonance images of the tumor site in mice. The *in vivo* study demonstrates that the injection of PFC-Q1@PLGA (O$_2$) into local tumors significantly enhances the radiotherapeutic effect on local tumors and also inhibits the growth of remote tumors by an enhanced abscopal effect. This study presents a novel radiotherapy strategy to enable synergistic whole-body therapeutic responses after localized treatment with PFC-Q1@PLGA (O$_2$).

Background

The tumor microenvironment plays an important role in the initiation and development of tumors.[1–3] It has been well established that a hypoxic microenvironment is a driving force for breast cancer progression and a contributing factor for a reduced therapeutic efficacy of radiotherapy.[4–8] As a strong radiosensitizer agent, oxygen can improve the radiosensitivity and the radiotherapeutic effect is closely correlated with the local oxygen

concentration.[9–11] Thus, reversing the hypoxic environment has become an effective interventional method to improve the oxygenation of tumor cells for oxygen-sensitized radiotherapy.[12–18]

Delivery of oxygen to tumors is a critical step for reversing the hypoxic tumor microenvironment.[19–22] One approach is to utilize nanoparticles or biofilm systems to encapsulate perfluorocarbons (PFCs) for targeted oxygen supply to tumors through the enhanced permeability and retention (EPR) effect since PFCs have been widely explored as an artificial blood substitute and an oxygen carrier due to their chemical and biological inertness,[23] ease of sterilization, and especially reliable biosecurity and extremely high oxygen solubility.[24–30] A change in the hypoxic environment by PFC-loaded systems could be significantly beneficial for the therapeutic effect of radiotherapy against breast tumors and the inhibitory effect on the metastasis of tumor cells.[31–34]

In addition, among all stromal cells that are present in the tumor microenvironment, tumor-associated fibroblasts (TAFs) are one of the most abundant and critical components of

[a] *Laboratory of Stem Cell Biology, and Huaxi MR Research Center (HMRRC), Department of Radiology, National Clinical Research Center for Geriatrics, West China Hospital, Sichuan University, Chengdu 610041, China.*
E-mail: luokui@scu.edu.cn, hyzhu_hmrrc@126.com
[b] *Research Unit of Psychoradiology, Chinese Academy of Medical Sciences, and Functional and molecular imaging Key Laboratory of Sichuan Province, Chengdu, 610041, China*
[c] *Amgen Bioprocessing Centre, Keck Graduate Institute, Claremont, CA 91711, USA*
†Electronic supplementary information (ESI) available. See DOI: 10.1039/d1nr03738b

mesenchymal tumors, which not only provide physical support for tumor cells, but also play a key role in promoting or retarding tumorigenesis in a context-dependent manner.[35–39] Previous reports have indicated that TAFs can express and secrete IL-25 after stimulation by lignan-derived compounds, and IL-25 can enhance the anticancer activity.[40,41] Lignans, widespread plant natural products, have various chemical structures and exhibit a myriad of biological activities.[42,43] A lignan-derived compound (Q1, methyl(*E*)-3-[2-(3,4-dihydroxy-phenyl)-7-hydroxy-3-methoxycarbonyl-2,3-dihydro-1-benzo furan-5yl] prop-2-enoate) has been shown to enhance the secretion of IL-25 from TAFs and in turn mediate a pronounced anti-metastatic effect.[40] However, the poor solubility of this small molecular compound in an aqueous solution and the lack of targeting ability have hampered its wide application in anti-tumor/anti-metastatic therapies.[44] This lignan-derived compound, Q1, as a IL-25 agonist was selected in this study for special mechanistic regulation of the tumor microenvironment to treat breast cancer, but an efficient delivery carrier needs to be developed for Q1.

Poly(lactic-*co*-glycolic acid) (PLGA) is a biodegradable polymer approved by the FDA as a pharmaceutical excipient and has been widely used in a large number of drug delivery systems.[45–47] PLGA can extend the duration of drug action and reduce side effects; meanwhile, it can simultaneously load many functional units with different properties to achieve combination therapy.[48,49] Herein, we chose PLGA as a carrier to encapsulate Q1 and perfluoro-15-crown-5 (PFC). We fabricated a co-delivery nanoplatform which was expected to tune the oxygen level and IL-25 secretion in the tumor microenvironment to enhance the radiotherapeutic effect against breast cancer and suppress the progress of distant tumors after the nanoplatform was delivered to the tumor site (Scheme 1). The characterization of the as-prepared nanoparticles was conducted *via* transmission electron microscopy (TEM), energy-dispersive X-ray spectroscopy (EDS) and dynamic light scattering (DLS). Stimulation of IL-25 secretion by the nanoparticles was evaluated in 3T3 fibroblasts and their *in vitro* antitumor effect was examined against 4T1 cells co-cultured with 3T3 fibroblasts. *In vivo* anti-local-tumor and anti-distant-tumor effects were assessed in 4T1 tumor-bearing mouse models. The results demonstrated that the PFC/Q1-encapsulated nanoparticles could tune the oxygen supply and IL-25 secretion in the tumor microenvironment to achieve meliorative tumor radiotherapy.
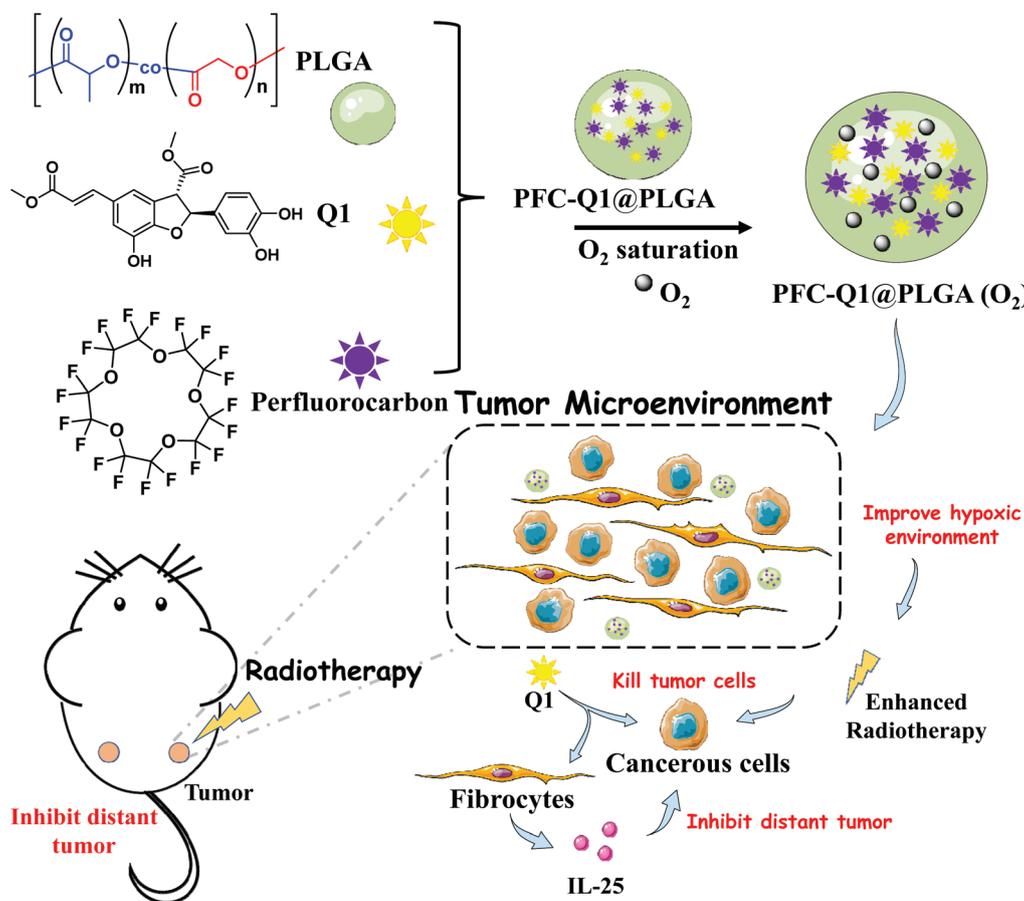
Scheme 1 Illustration of the preparation of a PLGA-based co-delivery nanoplatform for Q1 and PFC and its mechanism for meliorative tumor radiotherapy.

Materials and methods

Chemicals and materials

Poly(D,L-lactide-co-glycolide) (PLGA), polyvinyl alcohol (PVA), acetone, dichloromethane (DCM), and perfluoro-15-crown-5 were purchased from Sigma-Aldrich. Q1 (methyl(E)-3-[2-(3,4-dihydroxyphenyl)-7-hydroxy-3-methoxycarbonyl-2,3-dihydro-1-benzo furan-5yl] prop-2-enoate) was synthesized according to a previous report.[40] The cell counting kit (CCK-8) was purchased from MCE (USA), while the apoptosis analysis kit, cell cycle analysis kit and live/dead cell staining kit were purchased from Yeason (China).

Preparation of nanoparticles

10 mg of PLGA was dissolved in 400 μL of DCM, and 50 μL of PFC was added. 4 mL of 5% PVA in ddH$_2$O was added into the mixture solution while stirring. The solution was sonicated with a 20% power output in a controlled way of 3 s on/7 s off on ice for 5 min. Another 0.5 mL PVA solution was added, and the obtained mixture in an open vessel was stirred for 5 h at room temperature to vaporize organic solvents. The product was centrifuged at 16 000 rpm for 10 min at 4 °C, and then washed with PBS three times to remove PVA residues. The final PFC@PLGA product was collected, freeze-dried and stored at 4 °C for future use. To prepare Q1@PLGA, 5 mg of Q1 dissolved in 10 μL of acetone was added into 400 μL of DCM with 10 mg of PLGA. To prepare PFC-Q1@PLGA, 50 μL of PFC and 10 μL of acetone with 5 mg of Q1 were added into 400 μL of DCM with 10 mg of PLGA. 1 mg of Cy5.5 was added to prepare fluorescence-labeled nanoparticles.

Characterization of the nanoparticles

Elemental analysis of the nanoparticles was performed via energy-dispersive X-ray spectroscopy (EDS, Bruker 5030, Germany). The morphology of the nanoparticles was observed via transmission electron microscopy (TEM, FEI Tecnai GF20STWIN, USA). UV-vis spectra were recorded on a UV-Vis spectrophotometer (Shimadzu UV-1800, Japan). The size and zeta potential of the nanoparticles were measured via dynamic light scattering (DLS) (Brookhaven Omni, USA).

Evaluation of the encapsulation rate of Q1

The prepared nanoparticles were dissolved in DMSO, and the amount of Q1 in the nanoparticles was determined via a UV-vis spectrophotometer at 330 nm. The concentration in the supernatant was used to calculate the drug loading content and entrapment efficiency (loading content = weight of drug in nanoparticle/weight of nanoparticle × 100%; entrapment efficiency = weight of drug in nanoparticle/initial weight of drug × 100%). Different concentrations (50, 20, 10, 5 and 1 μg mL^{-1}) of Q1 were used for building a standard curve.

Cell lines and animals

4T1 cells were cultured at 37 °C with 5% CO$_2$ in tissue culture flasks with the Roswell Park Memorial Institute (RPMI) 1640 Medium supplemented with 10% bovine growth serum (Gemini, USA) and 1% penicillin–streptomycin (Hyclone, USA). All animal experiments were strictly carried out in accordance with the guidelines for animal studies approved by the Ethics Committee of West China Hospital, Sichuan University (2018154A). Mice were purchased from Chengdu Dossy Experimental Animals Co., Ltd.

Cellular cytotoxicity assessment

The 4T1 cells (5×10^3 per well) were planted and cultured in a 96 well plate for 12 h, and they were treated with free Q1 at different concentrations. After incubation for 24 h, the spent medium was discarded, and a 10% CCK-8 medium was added to assess the cell viability. A microplate reader (BioTek, USA) was used to record the absorbance at 450 nm for each well. Cells without treatment were used as a control. Results were presented as the mean cell viability normalized with that of the control group.

Cell apoptosis analysis

The apoptosis efficacy was evaluated by using a flow cytometer with a YF®488-Annexin V and PI Apoptosis Kit (Yeasen, China). Briefly, after the cells were treated with the nanoparticles at an equal concentration in a 6-well culture plate, they were harvested and suspended in the Annexin V binding buffer. The cells were then stained with a dye mixture (YF488-AnnexinV and Propidium Iodide, PI). Apoptosis was assessed by identifying viable, apoptotic, and necrotic cells with a flow cytometer (Canto, BD, USA). The level of apoptosis was analyzed by using the FlowJo V10 software.

Cell cycle analysis

The cell cycle was distinguished by using a flow cytometer with a cell cycle and apoptosis analysis kit (Yeasen, China) according to the manual. After the cells were treated with the nanoparticles, they were harvested and washed twice with PBS. 1 mL of pre-cooled 70% ethanol was added to the cells in an ice bath. After they were gently pipetted to mix, the cells were fixed at 4 °C for 24 h. The cells were carefully washed with cold PBS and stained with PI for 30 min at 37 °C. Then the cells were detected with a flow cytometer (Canto, BD, USA) in a PE channel. The cell cycle data were analyzed by using the Modfit software.

Live and dead cell staining of 3D tumor spheroids

Live and dead cell staining was performed under a fluorescent microscope with a Calcein-AM/PI Kit (Yeasen, China). 4T1 cells at 2×10^3 cells per well were seeded and incubated in a 96 U-bottom plate (Thermo Fisher Scientific, USA) for 48 h to form 3D tumor spheroids. 3T3 cells were incubated with the nanoparticles for 12 h and the conditional 3T3 culture medium was added to tumor spheroids and incubated for another 12 h. The cells were stained according to the instruction of the kit. They were incubated with the kit for 25 min and washed twice with PBS. The live and dead cells were observed by using a laser confocal fluorescent microscope. The normal 3T3 culture medium mixed with the nanoparticles at

the same concentration was added to 3D tumor spheroids as controls.

Western blot analysis of IL-25 expression

3T3 cells were treated with PFC-Q1@PLGA, Q1@PLGA, PFC@PLGA or control agents with 5 μg mL^{-1} Q1 for 48 h. The cells were collected and cell lysates were prepared with a RIPA buffer (no. R0010, Solarbio, China). After lysis, the supernatant was collected by centrifugation, and the loading buffer was added and boiled for western blot electrophoresis. β-Actin antibodies were purchased from Cell Signaling Technology (no. 3700T) and IL-25 antibodies from Affinity Biosciences (no. DF2528).

Measurement of dissolved oxygen in the nanoparticles

The dissolved oxygen in the nanoparticles was detected *via* a portable dissolved oxygen meter (JPBJ-608, INESA Scientific Instrument Co., Ltd, Shanghai, China). 1 mL of a nanoparticle solution at 5 mg mL^{-1} was added to a sample tube, and then subjected to pure oxygen saturation for 2 min. The above solution was injected into 5 mL of deoxygenated distilled water that was prepared by boiling under a nitrogen atmosphere and the oxygen concentrations in the solution were measured before and after the injection. In addition, distilled water was set as a control group.

Oxygenation determination by functional magnetic resonance imaging

The mice with tumors were anesthetized with isoflurane and fixed on the MRI (7T, Bruker, Germany) bed. After the baseline images were acquired, the mice were injected with PFC-Q1@PLGA. A series of images were acquired with the following parameters: TR = 30 ms, TE = 5 ms, FOV = 20 mm × 20 mm, matrix = 384 × 384, and scan time = 38 s. The data were analyzed with the Metalab software.

Accumulation of nanoparticles in tumors

To evaluate the accumulation of nanoparticles in a tumor site, the Cy5.5-labeled nanoparticles were prepared and injected into mice bearing tumors. After injection, the fluorescence intensity of Cy5.5 in the tumors was detected *via* an *in vivo* imaging system (IVIS, Caliper Life Sciences, USA) at 10 min, 30 min, 1 h, 3 h, and 5 h post-injection. Major organs were collected and imaged. The tumor tissues were collected, frozen sliced and imaged with a fluorescent microscope.

In vivo treatment with the nanoparticles and radiation

Mice were subcutaneously inoculated with 4T1 cells (1 × 10^6) in the right flank. About 7 days after implantation, animals with a tumor size of 50 mm^3 were used for antitumor studies. The mice were randomly divided into four groups, and injected with oxygen-saturated Q1@PLGA and PFC-Q1@PLGA at 100 μg Q1 per kg, and PFC@PLGA at the same PFC concentration as PFC-Q1@PLGA *via* the tail vein. Saline was injected as a control. After 1 h of post-injection, one half of the mice of each group (*n* = 5) were anesthetized with pentobarbital. Only tumors were exposed to 3 Gy X-ray radiation by cover-

ing other body parts with a lead plate. The mice were treated every two days and 3 times in total. The tumor size and mice body weight were measured every two days. Tumor volumes were calculated using the following formula: $V = L \times W^2 \times 0.5$, where V, L, and W are the tumor volume, length and width of the tumors, respectively.

To explore the therapeutic effect of the nanoparticles on distant tumors, the mice were subcutaneously inoculated with 4T1 cells in the left and right flank. About 7 days after implantation, the animals were used for antitumor studies. The oxygen-saturated nanoparticles and controls were *in situ* injected into the tumors on the right flank and the tumors on the right flank were exposed to X-ray radiation. The mice were treated every two days and 3 times in total. The tumor size at both sides and the mice body weight were measured every two days.

Statistical analysis

Statistical analysis was carried out by student's *t* test for two groups and one-way ANOVA for more than two groups. Data were presented as mean ± SD. $p < 0.05$ and $p < 0.01$ referred to statistical significance and high significance, respectively.

Results and discussion

The nanoparticles were characterized *via* TEM and DLS and the results are shown in Fig. 1. From the TEM images, all nanoparticles could be clearly observed after negative staining, and the Q1@PLGA nanoparticles (Fig. 1a, 78 nm) were smaller than PFC@PLGA (Fig. 1b, 110 nm) and PFC-Q1@PLGA (Fig. 1c, 120 nm). The hydrodynamic size and zeta potential of these nanoparticles were measured in water. The hydrodynamic sizes of Q1@PLGA, PFC@PLGA and PFC-Q1@PLGA were 87.1 nm, 123.2 nm and 160.6 nm, respectively (Fig. 1d and S3†). The zeta potentials of the three nanoparticles were similar (about −13.2 mV, Fig. 1f). The stability of the three nanoparticles was evaluated *via* detection of any changes in the size and zeta potential. After incubation of these nanoparticles with the DMEM cell medium, the size of the nanoparticles was detected at different time points. The hydrodynamic size had a negligible variation over the span of 72 h (Fig. 1e), which indicated the great stability of the as-prepared nanoparticles in the aqueous solution. Negligible changes were also seen in the zeta potential of these nanoparticles (Fig. 1g).

Different components in the three nanoparticles were distinguished *via* EDS. C and O elements were detected in the Q1@PLGA nanoparticles (Fig. 2a), while except for C and O elements, the F element was distinguished in both PFC@PLGA (Fig. 2b) and PFC-Q1@PLGA (Fig. 2c) nanoparticles. The results confirmed that PFC was encapsulated in the PFC@PLGA and PFC-Q1@PLGA nanoparticles. ^{18}F MRS in three nanoparticles was also measured in 5% D$_2$O water. The peak at around −91.93 ppm belong to perfluoro-15-crown-5 was detected in PFC@PLGA (Fig. 2e) and PFC-Q1@PLGA
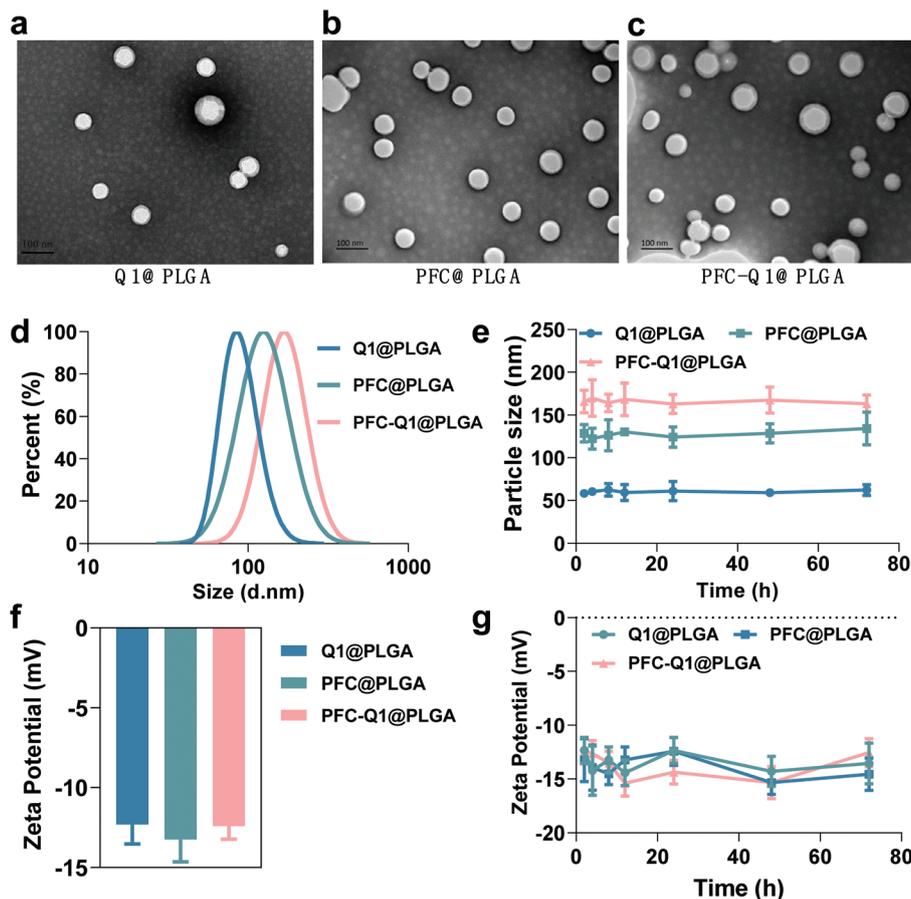
Fig. 1 Characterization of nanoparticles. (a–c) TEM images of Q1@PLGA, PFC@PLGA and PFC-Q1@PLGA (scale bar: 100 nm). (d) Hydrodynamic sizes of three nanoparticles measured by DLS. (e) Colloidal stability of nanoparticles in DMEM containing 10% FBS. (f) Zeta potentials of three nanoparticles. (g) Stability of nanoparticles in water.

(Fig. 2f), instead of Q1@PLGA (Fig. 2d). In addition, high resolution mass spectrometry (HRMS) of PFC-Q1@PLGA revealed that Q1 was encapsulated in the PLGA nanoparticles since there was a peak at $m/z = 387.1080\ [\text{M} + \text{H}]^+$ (Fig. S1†). According to the above results, three nanoparticles were successfully prepared. The UV spectra of Q1 and the nanoparticles were recorded by using a UV spectrophotometer (Fig. 2g) and Q1@PLGA (100.0 μg mL^{-1}) and PFC-Q1@PLGA (50.0 μg mL^{-1}) had an equivalent concentration of Q1 2.5 μg mL^{-1}. The Q1 loading rate in the Q1@PLGA and PFC-Q1@PLGA nanoparticles was estimated from a standard curve (Fig. S2†). The Q1 loading rate of Q1@PLGA and PFC-Q1@PLGA was 2.8% and 5.4%, respectively. The incorporation of PFC in PLGA improved its loading capacity for Q1, suggesting that fluorine could facilitate the assembly of the nanoparticles and maintain the stability of the nanoparticles.

The cell toxicity of the nanoparticles was analyzed *via* a CCK-8 kit. As shown in Fig. 3a, the half maximal inhibitory concentration (IC$_{50}$) of Q1 was 0.53 μM. From the results, the lignan derivative alone could inhibit the growth of 4T1 cells. To further identify the causes of cell toxicity, the changes in the cell cycle and the mitochondrial membrane potential were

measured. In cell cycle analysis (Fig. 3b), based on the propidium iodide (PI) staining of the cellular DNA content, the cells were significantly arrested in the G2/M phase (4n) when they were treated with Q1@PLGA and PFC-Q1@PLGA. Quantitative analysis indicated that the percentage of cells in the G2 phase after incubation with Q1@PLGA and PFC-Q1@PLGA was 72.6% and 67.1%, respectively, which were significantly higher than those in the control and PFC@PLGA-treated cells (18.3%) (Fig. 3c). The cell treated with PFC@PLGA had similar cell cycle as the cells without any treatment. This result indicated that Q1 played an important role in cell cycle alteration. A decrease in the mitochondrial membrane potential is also a landmark indicator in the early stage of apoptosis. The green fluorescence intensity significantly increased, while the red one decreased after treatment with the Q1@PLGA and PFC-Q1@PLGA nanoparticles compared with those in the PFC@PLGA-treated group and the control group, which demonstrated that the membrane potential of cells decreased after exposure to the Q1@PLGA and PFC-Q1@PLGA nanoparticles (Fig. 3e). As shown in the quantitative analysis results (Fig. 3d), the ratio of red/green fluorescence in the Q1@PLGA and PFC-Q1@PLGA treated cells was 0.9 ± 0.3 and 1.2 ± 0.2,
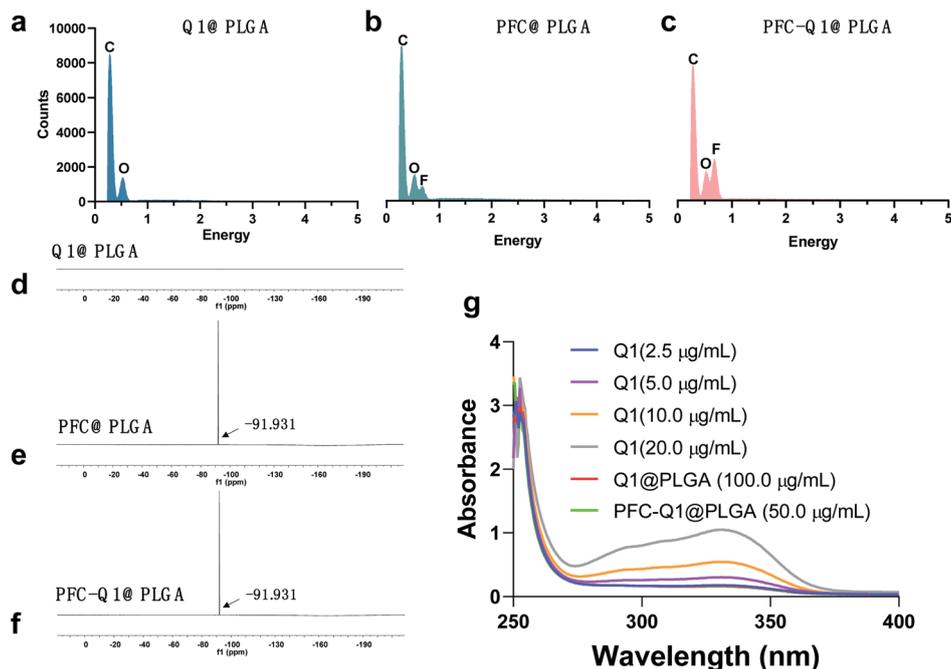
Fig. 2 (a–c) EDS of three nanoparticles. (d–f) ^{18}F MRS spectra of three nanoparticles. (g) UV spectra of Q1 and nanoparticles at gradient concentrations. The curves of Q1@PLGA (100.0 µg mL^{-1}) and PFC-Q1@PLGA (50.0 µg mL^{-1}) were overlapped with that of Q1 (2.5 µg mL^{-1}).
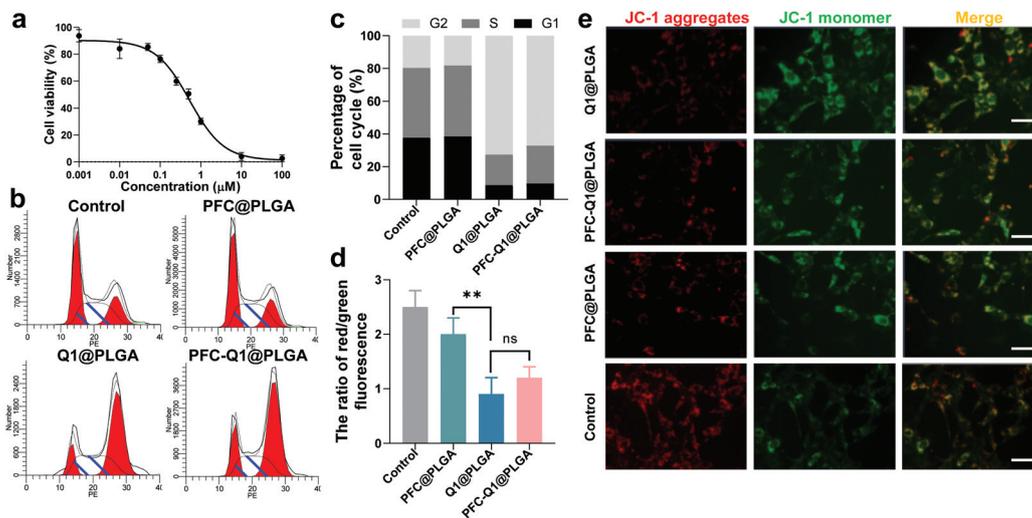

Fig. 3 (a) Cell cytotoxicity of Q1 in 4T1 cells. (b) Cell cycle alteration in 4T1 cells after incubation with nanoparticles. (c) Quantitative analysis of cell cycle alterations in 4T1 cells. (d) Quantitative analysis of the ratio of red to green fluorescence on the mitochondrial membrane in 4T1 cells after incubation with three nanoparticles. (e) Fluorescence images for indicating the mitochondrial membrane potential after incubation with nanoparticles (scale bar: 50 µm) (^{ns} $p > 0.05$, ** $p < 0.01$).

respectively, which were significantly smaller than those in the control and PFC@PLGA-treated cells ($p < 0.01$).

It has been reported that Q1 can greatly enhance the secretion of IL-25 in TAFs, resulting in a potent therapeutic effect against the surrounding carcinoma cells.[34] In this study, the fibroblast-NIH/3T3 cells were used to evaluate the secretion effect induced by Q1. Live/dead cell staining of 3D tumor spheroids was conducted to confirm the therapeutic enhance-

ment of the nanoparticles. The results shown in Fig. 4 indicated that much more dead cells (red fluorescence) were detected in 3D tumor spheroids after treatment with a 3T3 conditional culture medium (Fig. 4a), while there were less dead cells in tumor spheroids after exposure to a normal 3T3 culture medium with the nanoparticles (Fig. 4b). In this experiment, Q1 might stimulate 3T3 to generate IL-25, which was recently reported to confer a high anticancer activity and
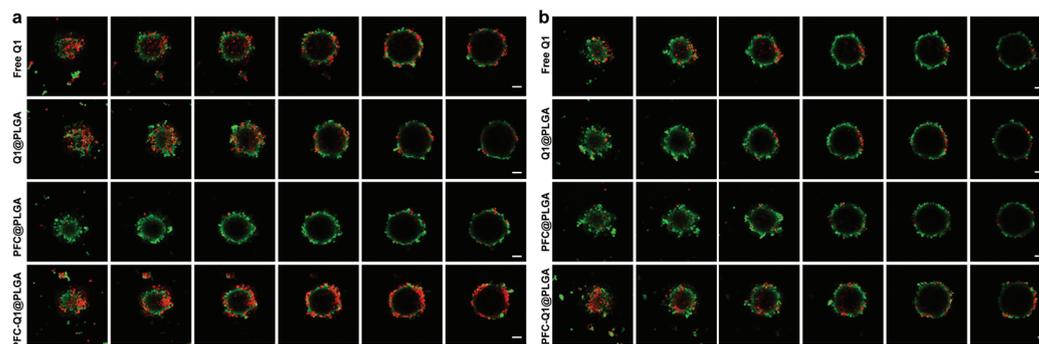
Fig. 4 (a) Live/dead cell staining images of 3D 4T1 cell spheroids after incubation with a 3T3 conditional culture medium which was harvested after incubation of 3T3 cells with nanoparticle-containing cell culture for 12 h (scale bar: 100 μm). (b) Live/dead cell staining images of 3D 4T1 cell spheroids after incubation with a normal 3T3 culture medium mixed with nanoparticles (scale bar: 100 μm).

increase the therapeutic efficacy. These results confirmed that the nanoparticles could enhance the killing effect on tumor cells after interaction with fibroblast cells.

As shown in Fig. 5a, the apoptosis of 3T3^{GFP}cells, 4T1 cells and 4T1 cells co-cultured with 3T3^{GFP} after treatment with the nanoparticles was analyzed by using a flow cytometer. Very few apoptotic cells were detected in 3T3 cells after incubation with the nanoparticles, which suggested that these nanoparticles were not cytotoxic to 3T3 cells. However, a large population of late apoptotic cells were detected in the nanoparticle-treated 4T1 cells (Q2 quadrant), and the level of apoptosis in the 4T1 cells co-cultured with or without 3T3 cells was quite different (free Q1, $25.9 \pm 5.4\%$ (w) $vs.$ $19.8 \pm 3.4\%$ (w/o), Q1@PLGA $26.5 \pm 4.5\%$ (w) $vs.$ $13.3 \pm 4.3\%$ (w/o), PFC-Q1@PLGA $31.5 \pm 4.9\%$ (w) $vs.$ $18.9 \pm 2.3\%$ (w/o), $p < 0.01$). A consistent pattern in the number of late apoptosis cells was found in the 4T1 cells after incubation with free Q1 and the Q1-incorporated nanoparticles when they were co-cultured with 3T3 cells (Fig. 5b). The results demonstrated that either free Q1 or Q1 in the nanoparticles could enhance the therapeutic effect against 4T1 cells by co-

culture with 3T3 cells. Different percentages of early apoptosis in 4T1 cells may be due to the cellular uptake of free Q1 or Q1-incorporated nanoparticles in 4T1 cells. Western blot was used to evaluate the expression of IL-25 in the 3T3 cells after incubation with free Q1, Q1@PLGA and PFC-Q1@PLGA. As shown in Fig. 5c, a higher expression level of IL-25 was detected in the PFC-Q1@PLGA- and Q1@PLGA-treated groups in comparison with those in the control and PFC@PLGA groups. Quantitative analysis results in Fig. S3† confirmed that the concentration of IL-25 in the PFC-Q1@PLGA- and Q1@PLGA-treated 4T1 cells was 1.4 fold higher than those in the control and PFC@PLGA groups.

It has been demonstrated that PFC has a high oxygen-carrying ability, and it was hypothesized that the PFC-encapsulated nanoparticles could deliver oxygen to the tumor site. The oxygen release behavior from the nanoparticles was assessed in aqueous solutions via a portable dissolved oxygen probe to determine the dissolved oxygen concentration. As shown in Fig. 6a, the dissolved oxygen concentration was increased in deoxygenated distilled water after the addition of oxygen-satu-
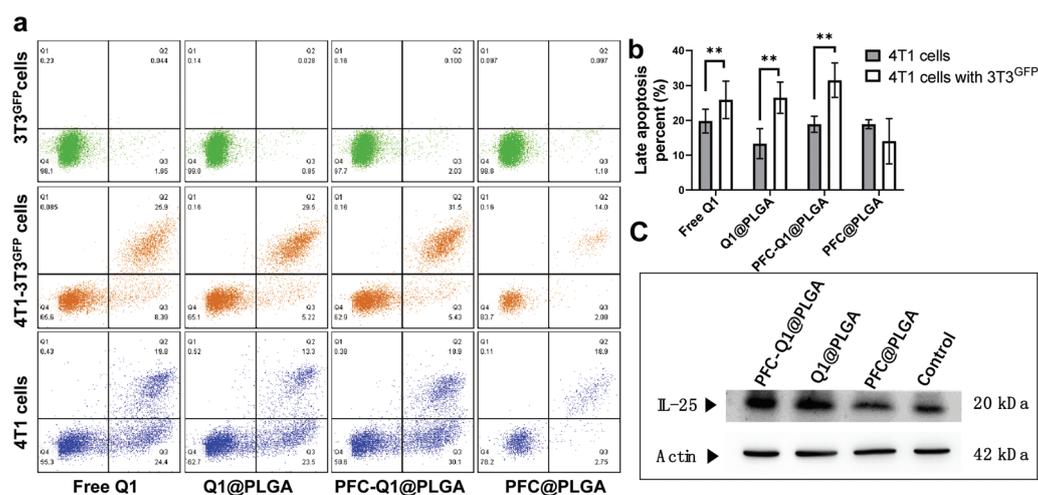

Fig. 5 (a) Apoptosis of 3T3^{GFP}, 4T1-3T3^{GFP} and 4T1 cells after incubation with free Q1 and various nanoparticles. (b) Quantitative analysis of the late apoptosis percentage in different cell groups. (c) The expression of IL25 in 3T3 cells after incubation with nanoparticles (** $p < 0.01$).
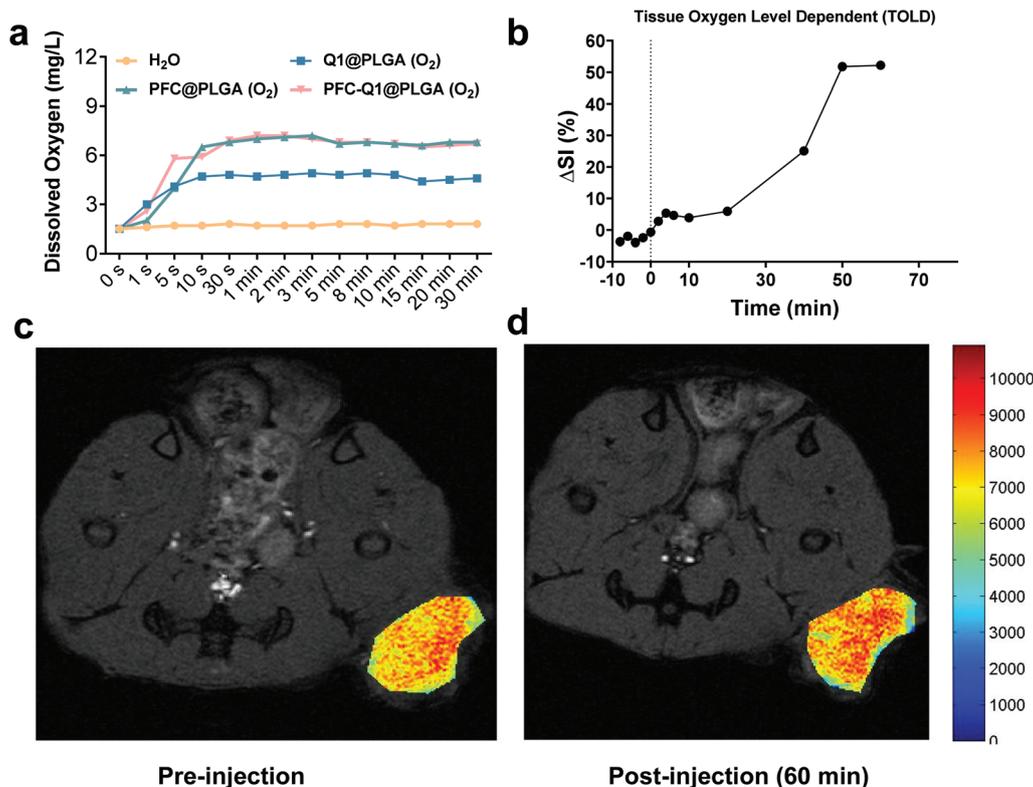
Fig. 6 (a) Dissolved oxygen concentrations in the nanoparticle solutions after oxygen saturation. (b) MR signal intensity alterations at the tumor site before and after the injection of an oxygen saturated solution of PFC–Q1@PLGA (O_2). (c) MR images of the tumor site before injection of an oxygen saturated solution of PFC–Q1@PLGA (O_2). (d) MR images of the tumor site after injection of an oxygen saturated solution of PFC–Q1@PLGA (O_2).

rated nanoparticles. Within 1 min, the dissolved oxygen concentration rapidly increased from 1.5 mg L^{-1} to 7.0 mg L^{-1} and 7.2 mg L^{-1} after the PFC@PLGA and PFC-Q1@PLGA nanoparticles were added, respectively. The oxygen concentration remained unchanged during the next 30 min. However, the oxygen concentration increased to 4.7 mg L^{-1} in the Q1@PLGA group in 10 s and remained unchanged after 10 s. The results demonstrated that the PFC@PLGA and PFC-Q1@PLGA nanoparticles had an excellent oxygen-carrying ability. Inspired by an excellent oxygen-carrying ability of the PFC-Q1@PLGA nanoparticles, we quantified signal intensity alterations in the tissue oxygen level dependent (TOLD) signals at the tumor site after injection of the oxygen-saturated nanoparticles by functional magnetic resonance imaging (fMRI). Previous studies have demonstrated that the T1 signal changes of MRI are responsive to an increased oxygen content in tumor tissues, and TOLD signals primarily depend on the oxygen pressure in the tissue.[50–52] From the imaging results, the T1-measured signal intensity was significantly increased after the injection of the oxygen-saturated nanoparticles, up to about 52.3% in 60 min (Fig. 6b–d).

To evaluate the accumulation of the nanoparticles in tumor cells, the Cy5.5-labeled nanoparticles were prepared and injected into mice bearing tumors. As shown in Fig. 7a, the fluorescence signal at the tumor site was recorded at different time points after injection. Semi-quantitative analysis results

of the fluorescence intensity in tumors are shown in Fig. S5.†
At 30 min post-injection, the fluorescence signal was detectable in the mice injected with three nanoparticles, which indicated that these nanoparticles started to accumulate at the tumor site. The fluorescence signal was continuously intensified with time, and there was no significant difference in the signal at the tumor site of the mice injected with three nanoparticles. The results demonstrated that the three nanoparticles had a similar accumulation level at the tumor site. Major organs were collected and detected by fluorescence imaging (Fig. 7b). A strong fluorescence signal was detected in the tumor tissue, which confirmed the accumulation of PFC-Q1@PLGA-treated tumors rather than in other organs. The fluorescence signal in the tumor tissue sections was further observed under a microscope (Fig. 7c); a higher level of accumulation of PFC-Q1@PLGA in tumor tissues could help achieving better therapeutic effects of PFC-Q1@PLGA.

The 4T1 murine breast cancer model was employed to investigate the *in vivo* antitumor activity of the nanoparticles in combination with radiation. The therapeutic effect was firstly evaluated after the intravenous injection of the nanoparticles into mice through monitoring the mice body weight and measuring the tumor volume during the experimental period. All nanoparticles were oxygenated before injection. As shown in Fig. 8a and b, the tumor volume in the Q1@PLGA- or PFC-Q1@PLGA-treated group without radiation was similar to
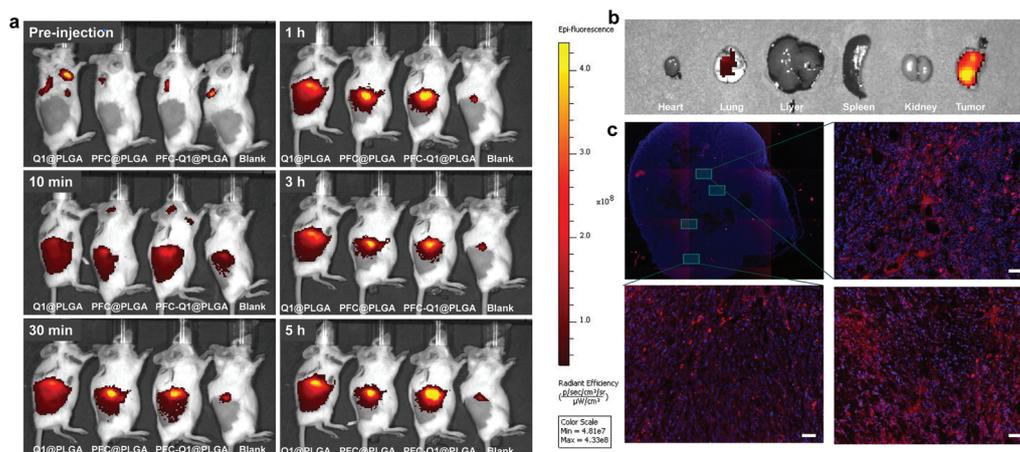
Fig. 7 (a) Accumulation of Cy5.5-labelled nanoparticles in tumor cells. (b) Fluorescence images of major organs in the PFC-Q1@PLGA-treated group by IVIS. (c) Fluorescence images of tumor tissues in the PFC-Q1@PLGA treated-group under a microscope (scale bar: 200 μm).
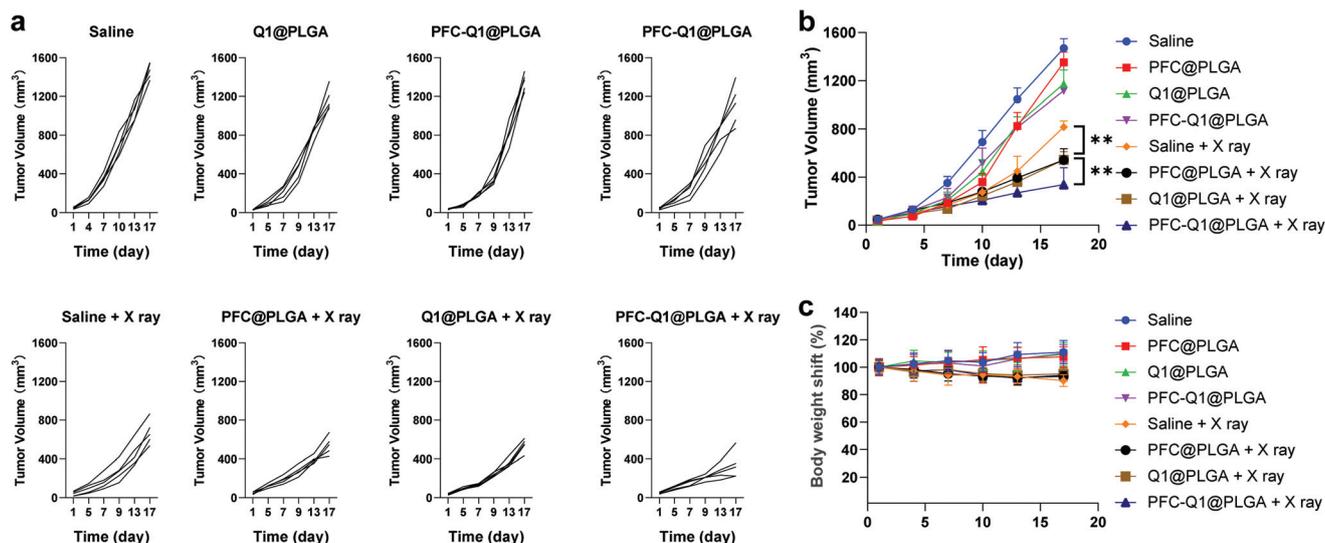

Fig. 8 (a) Individual tumor growth kinetics in different treatment groups after intravenous injection. (b) Average tumor growth kinetics in different treatment groups after intravenous injection; data were presented as mean ± s.e. ($n = 5$). (c) Body weight shifts of mice during the treatment period; data were presented as mean ± s.e. ($n = 5$) (** $p < 0.01$).

those in the PFC@PLGA- and saline-treated groups, while the tumors significantly shrank in the mice after radiotherapeutic treatment in conjunction with the injection of Q1@PLGA- or PFC-Q1@PLGA in comparison with tumors in the PFC@PLGA- and saline-treated groups, which indicated that the incorporation of Q1 in the nanoparticles could enhance the radiotherapeutic effect against breast tumors *in vivo*. The tumor volume in the PFC@PLGA-treated group was 541.7 ± 94.1 mm³, which was smaller than that in the saline-treated group after radiation. The results indicated that a high oxygen level could help boosting the therapeutic effect of radiation, which was further confirmed by comparing an average tumor volume of 337.2 ± 140.2 mm³ in the PFC-Q1@PLGA-treated group with a tumor volume of 543.6 ± 67.8 mm³ in the Q1@PLGA-treated group at

the same radiation dosage. The results confirmed our hypothesis that the incorporation of Q1 for enhancing IL-25 secretion from fibroblasts in the tumor tissue and PFC for increasing the oxygen level in the tumor microenvironment in the PLGA nanoparticles could significantly strengthen the radiotherapeutic efficacy and reduce the volume of breast tumors. Negligible shifts in the mice body weight indicated that these nanoparticles had no/low side effects after systemic injection (Fig. 8c).

In radiation therapy, an abscopal effect is described as the shrinkage of tumors away from the region of localized radiotherapeutic treatment, which may be induced by immune responses after irradiation. In this experiment, we also investigated the therapeutic effect of these nanoparticles on distant
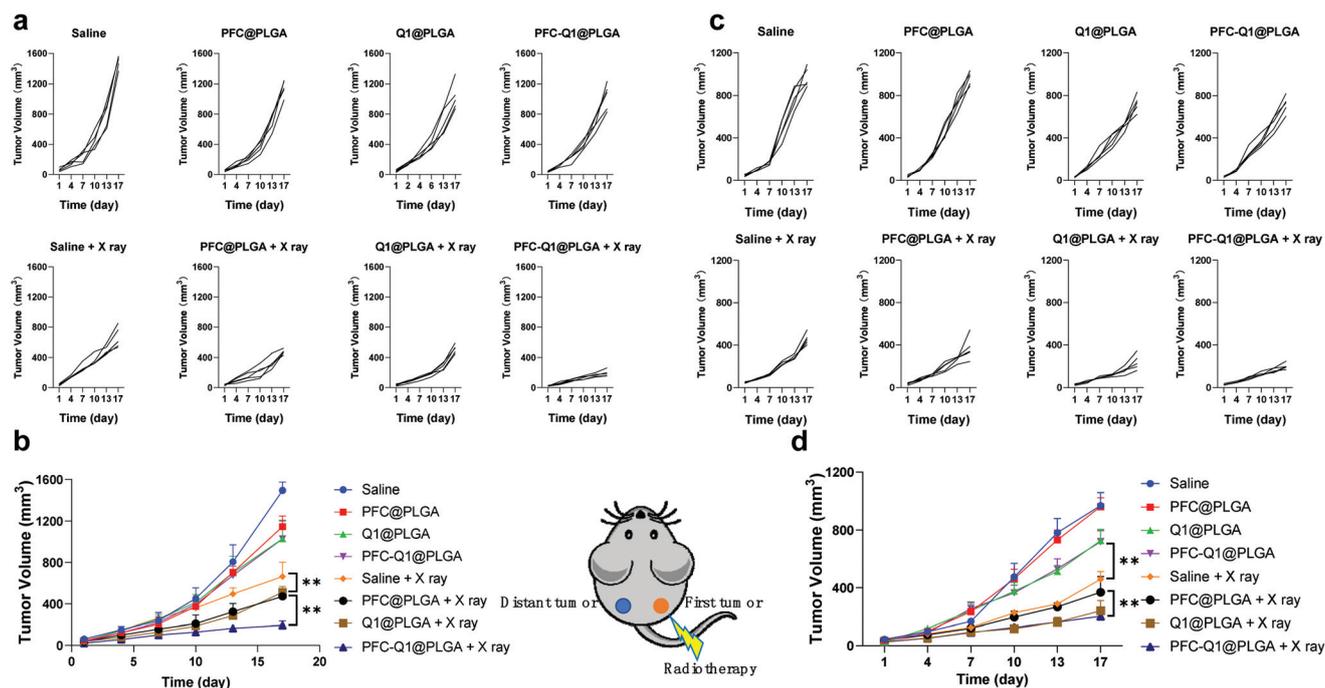
Fig. 9 (a) Individual growth kinetics of tumors on the right side in different treatment groups after *in situ* injection. (b) Average growth kinetics of tumors on the right side in different treatment groups after *in situ* injection; data were presented as mean ± s.e. (*n* = 5). (c) Individual growth kinetics of tumors on the left side (distant tumor) in different treatment groups. (d) Average growth kinetics of tumors on the left side (distant tumor) in different treatment groups; data were presented as mean ± s.e. (*n* = 5) (** *p* < 0.01).

tumors. Tumor cells were located in both right and left flank of the mice. After the treatment of tumors on the right side by the injection of nanoparticles into them with radiation, the tumor volume on both sides was recorded and analyzed. The tumor volume changes for those *in situ* treated tumors (right side) were similar to those after intravenous treatment, and the PFC-Q1@PLGA-treated group with radiation displayed the best therapeutic effect (Fig. 9a and b). The PFC-Q1@PLGA-treated group with radiation had an average tumor volume of 192.6 ± 42.8 mm^3 on day 17, which was significantly smaller than that of 512.3 ± 54.8 mm^3 in the Q1@PLGA-treated group and that of 472.8 ± 31.1 mm^3 in the PFC@PLGA-treated group. It was evident that the volume of distant tumors on the left side without any treatment shrank during the experimental period. As shown in Fig. 9c and d, the tumor volumes in the Q1@PLGA and PFC-Q1@PLGA groups without radiation were significantly smaller than those in other two groups, which suggested that the treatment with Q1@PLGA and PFC-Q1@PLGA nanoparticles could inhibit the growth of distant tumors. Due to the "abscopal effect", the radiation of tumors on the right side also inhibited the growth of distant tumors on the left side for all groups receiving the nanoparticles and the control group. The Q1@PLGA- (240.8 ± 71.0 mm^3) and PFC-Q1@PLGA-treated groups (202.0 ± 29.9 mm^3) after radiation displayed a better inhibitory effect than other two groups, indicating that the Q1-encapsulated nanoparticles could help enhancing the inhibitory effect of

radiation. The therapeutic outcomes for distant tumors after treatment with the PFC/Q1-encapsulated nanoparticles in the 4T1 tumor models confirmed that a high oxygen level and IL-25 secretion in the tumor microenvironment might strengthen the abscopal effect of radiotherapy.

Conclusions

We have constructed a co-delivery nanoplatform for a lignan-derived compound Q1 and perfluorocarbon to increase IL-25 secretion and the oxygen level in the tumor microenvironment, resulting in an enhancement in the tumor-killing effect by radiation. Treatment with Q1-encapsulated nanoparticles led to significant changes in the cell cycle and mitochondrial membrane potentials, an increase in the expression of IL-25 from fibroblasts and a high level of apoptosis in tumor cells. The MR images of a tumor site revealed that the tissue oxygen level in tumors was significantly improved after injection of oxygen-saturated nanoparticles. Our *in vivo* study confirmed that treatment with the Q1/PFC-incorporated nanoparticles could significantly boost the radiotherapeutic effect and suppress the progress of distant tumors in breast cancer. This study provides a new strategy for manipulating the tumor microenvironment to improve the radiotherapeutic efficacy on *in situ* and distant tumors.

Conflicts of interest

There are no conflicts to declare.

Acknowledgements

References

1 L. A. Liotta and E. C. Kohn, *Nature*, 2001, **411**, 375–379.
2 A. Albini and M. B. Sporn, *Nat. Rev. Cancer*, 2007, **7**, 139–147.
3 L. De Mattos-Arruda, J. Cortes, J. Blanco-Heredia, D. G. Tiezzi, G. Villacampa, S. Gonçalves-Ribeiro, L. Paré, C. A. Souza, V. Ortega, S.-J. Sammut, P. Cusco, R. Fasani, S.-F. Chin, J. Perez-Garcia, R. Dienstmann, P. Nuciforo, P. Villagrasa, I. T. Rubio, A. Prat and C. Caldas, *NPJ Breast Cancer*, 2021, **7**, 73.
4 M. R. Horsman, L. S. Mortensen, J. B. Petersen, M. Busk and J. Overgaard, *Nat. Rev. Clin. Oncol.*, 2012, **9**, 674–687.
5 L. Zhao, C. Fu, L. Tan, T. Li, H. Zhong and X. Meng, *Nanoscale*, 2020, **12**, 2855–2874.
6 D. Xia, P. Xu, X. Luo, J. Zhu, H. Gu, D. Huo and Y. Hu, *Adv. Funct. Mater.*, 2019, **29**, 1807294.
7 V. Petrova, M. Annicchiarico-Petruzzelli, G. Melino and I. Amelio, *Oncogenesis*, 2018, **7**, 10.
8 J. A. C. M. Goos, M. Davydova, N. Lengkeek, I. Greguric, M. R. Whittaker, J. F. Quinn, J. B. Baell, J. S. Lewis and T. P. Davis, *Macromol. Rapid Commun.*, 2020, **41**, 2000061.
9 J. M. Thoday and J. Read, *Nature*, 1947, **160**, 608.
10 C. Liu, Q. Lin and Z. Yun, *Radiat. Res.*, 2015, **183**, 487–496.
11 D. L. Dewey, *Nature*, 1960, **186**, 780–782.
12 X. Song, L. Feng, C. Liang, K. Yang and Z. Liu, *Nano Lett.*, 2016, **16**, 6145–6153.
13 D. Huo, S. Liu, C. Zhang, J. He, Z. Zhou, H. Zhang and Y. Hu, *ACS Nano*, 2017, **11**, 10159–10174.
14 C. Bernauer, Y. K. S. Man, J. C. Chisholm, E. Y. Lepicard, S. P. Robinson and J. M. Shipley, *Br. J. Cancer*, 2021, **124**, 539–551.
15 N. Graf and S. J. Lippard, *Adv. Drug Delivery Rev.*, 2012, **64**, 993–1004.
16 H. Liu, Y. Cai, Y. Zhang, Y. Xie, H. Qiu, H. Hua, X. Liu, Y. Li, J. Lu, L. Zhang and R. Yu, *Adv. Healthcare Mater.*, 2017, **6**, 1601377.
17 H. Huang, C. Zhang, X. Wang, J. Shao, C. Chen, H. Li, C. Ju, J. He, H. Gu and D. Xia, *Nano Lett.*, 2020, **20**, 4211–4219.
18 S. Shi, R. Vissapragada, J. Abi Jaoude, C. Huang, A. Mittal, E. Liu, J. Zhong and V. Kumar, *Bioact. Mater.*, 2020, **5**, 233–240.
19 J. Liu, W. Bu and J. Shi, *Chem. Rev.*, 2017, **117**, 6160–6224.
20 Z. Zhou, B. Zhang, H. Wang, A. Yuan, Y. Hu and J. Wu, *Theranostics*, 2018, **8**, 4898–4911.
21 Z. Chen, L. Liu, R. Liang, Z. Luo, H. He, Z. Wu, H. Tian, M. Zheng, Y. Ma and L. Cai, *ACS Nano*, 2018, **12**, 8633–8645.
22 J. Zhuang, M. Ying, K. Spiekermann, M. Holay, Y. Zhang, F. Chen, H. Gong, J. H. Lee, W. Gao, R. H. Fang and L. Zhang, *Adv. Mater.*, 2018, **30**, 1804693.
23 M. A. Miller and E. M. Sletten, *ChemBioChem*, 2020, **21**, 3451–3462.
24 D. Hu, L. Zhong, M. Wang, H. Li, Y. Qu, Q. Liu, R. Han, L. Yuan, K. Shi, J. Peng and Z. Qian, *Adv. Funct. Mater.*, 2019, **29**, 1806199.
25 M. Sun, J. Lee, Y. Chen and K. Hoshino, *Bioact. Mater.*, 2020, **5**, 924–937.
26 H. Cai, X. Dai, X. Wang, P. Tan, L. Gu, Q. Luo, X. Zheng, Z. Li, H. Zhu, H. Zhang, Z. Gu, Q. Gong and K. Luo, *Adv. Sci.*, 2020, **7**, 1903243.
27 S. Guo, X. Wang, Y. Dai, X. Dai, Z. Li, Q. Luo, X. Zheng, Z. Gu, H. Zhang, Q. Gong and K. Luo, *Adv. Sci.*, 2020, **7**, 2000467.
28 Y. Wu, F. Li, X. Zhang, Z. Li, Q. Zhang, W. Wang, D. Pan, X. Zheng, Z. Gu, H. Zhang, Q. Gong and K. Luo, *Carbohydr. Polym.*, 2021, **255**, 117490.
29 X. Zhang, Y. Wu, Z. Li, W. Wang, Y. Wu, D. Pan, Z. Gu, R. Sheng, H. Tomás, H. Zhang, J. Rodrigues, Q. Gong and K. Luo, *Carbohydr. Polym.*, 2020, **247**, 116749.
30 N. L. Fletcher, K. Kempe and K. J. Thurecht, *Macromol. Rapid Commun.*, 2020, **41**, 2000319.
31 M. Gao, C. Liang, X. Song, Q. Chen, Q. Jin, C. Wang and Z. Liu, *Adv. Mater.*, 2017, **29**, 1701429.
32 N. Lu, W. Fan, X. Yi, S. Wang, Z. Wang, R. Tian, O. Jacobson, Y. Liu, B. C. Yung, G. Zhang, Z. Teng, K. Yang, M. Zhang, G. Niu, G. Lu and X. Chen, *ACS Nano*, 2018, **12**, 1580–1591.
33 L. Yao, L. Feng, D. Tao, H. Tao, X. Zhong, C. Liang, Y. Zhu, B. Hu, Z. Liu and Y. Zheng, *Nanoscale*, 2020, **12**, 14764–14774.
34 G. Song, C. Liang, X. Yi, Q. Zhao, L. Cheng, K. Yang and Z. Liu, *Adv. Mater.*, 2016, **28**, 2716–2723.

35 E. Sahai, I. Astsaturov, E. Cukierman, D. G. DeNardo, M. Egeblad, R. M. Evans, D. Fearon, F. R. Greten, S. R. Hingorani, T. Hunter, R. O. Hynes, R. K. Jain, T. Janowitz, C. Jorgensen, A. C. Kimmelman, M. G. Kolonin, R. G. Maki, R. S. Powers, E. Puré, D. C. Ramirez, R. Scherz-Shouval, M. H. Sherman, S. Stewart, T. D. Tlsty, D. A. Tuveson, F. M. Watt, V. Weaver, A. T. Weeraratna and Z. Werb, *Nat. Rev. Cancer*, 2020, **20**, 174–186.

36 A. Orimo, P. B. Gupta, D. C. Sgroi, F. Arenzana-Seisdedos, T. Delaunay, R. Naeem, V. J. Carey, A. L. Richardson and R. A. Weinberg, *Cell*, 2005, **121**, 335–348.

37 R. Kalluri, *Nat. Rev. Cancer*, 2016, **16**, 582–598.

38 J. Lang, X. Zhao, Y. Qi, Y. Zhang, X. Han, Y. Ding, J. Guan, T. Ji, Y. Zhao and G. Nie, *ACS Nano*, 2019, **13**, 12357–12371.

39 L. Miao, J. M. Newby, C. M. Lin, L. Zhang, F. Xu, W. Y. Kim, M. G. Forest, S. K. Lai, M. I. Milowsky, S. E. Wobker and L. Huang, *ACS Nano*, 2016, **10**, 9243–9258.

40 S.-Y. Yin, F.-Y. Jian, Y.-H. Chen, S.-C. Chien, M.-C. Hsieh, P.-W. Hsiao, W.-H. Lee, Y.-H. Kuo and N.-S. Yang, *Nat. Commun.*, 2016, **7**, 11311.

41 S. Apers, D. Paper, J. Bürgermeister, S. Baronikova, S. Van Dyck, G. Lemière, A. Vlietinck and L. Pieters, *J. Nat. Prod.*, 2002, **65**, 718–720.

42 L. Pieters, S. Van Dyck, M. Gao, R. Bai, E. Hamel, A. Vlietinck and G. Lemière, *J. Med. Chem.*, 1999, **42**, 5475–5481.

43 J. S. Bose, V. Gangan, R. Prakash, S. K. Jain and S. K. Manna, *J. Med. Chem.*, 2009, **52**, 3184–3190.

44 S. Wilhelm, A. J. Tavares, Q. Dai, S. Ohta, J. Audet, H. F. Dvorak and W. C. W. Chan, *Nat. Rev. Mater.*, 2016, **1**, 16014.

45 F. Hu, T. Yan, W. Guo, Q. Liu, M. H. Han, C. Liu, Y. Liu, W. Zheng, F. You, Y. Yang, W. Zhang and X. Ma, *Nanoscale*, 2020, **12**, 10623–10638.

46 S. Acharya and S. K. Sahoo, *Adv. Drug Deliv. Rev.*, 2011, **63**, 170–183.

47 J. Panyam and V. Labhasetwar, *Adv. Drug Deliv. Rev.*, 2012, **64**, 61–71.

48 Y. Yin, J. Wang, M. Yang, R. Du, G. Pontrelli, S. McGinty, G. Wang, T. Yin and Y. Wang, *Nanoscale*, 2020, **12**, 2946–2960.

49 W. Zhou, H. Yu, L. Zhang, B. Wu, C. Wang, Q. Wang, K. Deng, R. Zhuo and S. Huang, *Nanoscale*, 2017, **9**, 17044–17053.

50 K.-I. Matsumoto, M. Bernardo, S. Subramanian, P. Choyke, J. B. Mitchell, M. C. Krishna and M. J. Lizak, *Magn. Reson. Med.*, 2006, **56**, 240–246.

51 S. C. Beeman, Y.-B. Shui, C. J. Perez-Torres, J. A. Engelbach, J. J. H. Ackerman and J. R. Garbow, *Magn. Reson. Med.*, 2016, **75**, 2442–2447.

52 R. R. Hallac, H. Zhou, R. Pidikiti, K. Song, S. Stojadinovic, D. Zhao, T. Solberg, P. Peschke and R. P. Mason, *Magn. Reson. Med.*, 2014, **71**, 1863–1873.